

1 Gas-permeable carbon molecular sieve membranes
2 fabricated from a norbornene-functionalized
3 polyimide–polyhedral oligomeric silsesquioxane
4 composite

5 *Sulaiman O. Lawal, Kenta Watanabe, Ryohei Uchino, Norihiro Moriyama, Hiroki Nagasawa,*
6 *Toshinori Tsuru, and Masakoto Kanezashi**

7 Chemical Engineering Program, Graduate School of Advanced Science and Engineering,
8 Hiroshima University, 1-4-1 Kagamiyama, Higashi-Hiroshima 739-8527, Japan

9 *Corresponding author: E-mail address: kanezashi@hiroshima-u.ac.jp (M. Kanezashi)

Abstract

Polyhedral oligomeric silsesquioxanes (POSS) are a promising family of regularly structured silsesquioxanes with resilient cage-like configurations and exterior edges that can be functionalized with various organic groups. In this study, POSS was functionalized with a polyimide–phenylene (PI–Ph) unit, which yielded POSS–PI–Ph to fabricate carbonized POSS membranes (denoted as carbon-POSS) *via* inert pyrolysis. Replacing some PI–Ph units with norbornene (NB) increased the amount of residual carbon formed in the carbon-POSS structure. X-ray photoelectron spectroscopy and ^{29}Si nuclear magnetic resonance analysis revealed that residual sp^2 -hybridized carbon atoms were connected to the POSS cage after pyrolysis at 700 °C. Analysis of single-gas permeation at 200 °C with the carbon-POSS membranes pyrolyzed at different temperatures (200–800 °C) indicated that the permeance of all investigated gases (He, H_2 , CO_2 , N_2 , CH_4 , CF_4 , and SF_6) increased with increasing membrane pyrolysis temperature. Notably, the early onset of the decline in permeance of large-molecule gases such as CF_4 and SF_6 at 600 °C ensured a high N_2 permeance and ideal N_2/SF_6 selectivity of $10^{-6} \text{ mol m}^{-2} \text{ s}^{-1} \text{ Pa}^{-1}$ and 100, respectively. Overall, this study demonstrates the feasibility of preparing high-performance carbonized POSS-derived membranes by optimizing the NB functionality and POSS content of the hybrid copolymer precursor.

KEYWORDS: Polyhedral oligomeric silsesquioxane; norbornene; polyimide; carbon; retro Diels–Alder reaction; ring-opening metathesis; gas separation

1 Introduction

Silsesquioxanes are a unique group of compounds with the general formula $(\text{RSiO}_{3/2})_n$, where R denotes a hydrogen atom or an organic group such as alkyl, alkylene, aryl, arylene, and their organofunctional derivatives [1]. Silsesquioxanes exhibit diverse structures, such as random, ladder, and cage configurations [2]. In particular, cage-structured silsesquioxanes—which are referred to as polyhedral oligomeric silsesquioxanes (POSS) [2,3]—possess an inorganic–organic architecture comprising an inner inorganic $(\text{SiO}_{3/2})_n$ cage surrounded by organic moieties [3]. Consequently, POSSs have been used to synthesize various POSS–polymer composites with polymers such as polyimides (PIs), polyamides, polyethers, polyesters, polystyrenes, poly(methyl methacrylate)s [2,4], and polybenzoxazine [5].

Owing to the synergistic combination of POSS and polyimide moieties, POSS–PI composites have attracted considerable attention for various applications because of their distinctive properties, such as their excellent thermal and mechanical stability [2,4–6]. POSS–PI composites have recently been applied in systems such as electrical insulators [7], thermal shields [4,6,8], solar cells [9], color filters, conductive films [10], and separation membranes [11–14]. Particularly, POSS–PI composite membranes exhibiting different configurations have been studied. For instance, Dasgupta *et al.* [11] and Iyer *et al.* [13] investigated the gas transport properties of aminoethylaminopropylisobutyl–POSS- and octaamino–POSS-embedded PI mixed matrix membranes, respectively, in which functionalized POSS nanoparticles served as nanofillers in the PI superstructure, leading to macroscopic interactions. Additionally, Kanezashi *et al.* [14] and, more recently, Xiao *et al.* [15] explored molecularly integrated POSS–polymer composite membranes in which the POSS and PI moieties were combined in a copolymer network. Several

studies have suggested that integrating POSS and polymer moieties into a copolymer chain helps in fully realizing the benefits of both components of POSS–polymer composites [3–6,16].

Compositing PI and POSS can be leveraged to develop more thermally robust ceramics. POSS pyrolysis was first reported in 1985 by Chi, who synthesized a silicon oxycarbide (SiOC) with the formula $\text{SiO}_{1.5}\text{C}_{0.5}$ by pyrolyzing a POSS at 1200 °C in an argon atmosphere [1]. The resulting SiOC materials are considered porous polymer-derived ceramics, and their properties can be altered by rationally controlling aspects such as precursor composition, architecture, and pyrolysis conditions [17]. Similarly, PI pyrolysis products have been extensively studied as carbon molecular sieves (CMSs). Consequently, CMS membranes have been fabricated to separate CO_2 [18–20], H_2 [21,22], and C_3 gases [23,24], highlighting the advantages of CMSs for generating ultramicroporous microstructures; however, these systems exhibit low permeability and aging problems [22,25,26]. Therefore, the pyrolysis products of POSS–PI composites can help facilitate the fabrication of high-performance separation membranes, with the rigid POSS cage networks helping to alleviate the low permeability and aging of CMSs [16].

Previously, our group examined the permeation properties of a homogeneous-POSS-derived membrane fabricated at a pyrolysis temperature of 550 °C [27]. The caged structure of the POSS prevented the densification of the siloxane linkages, which occurred in the corresponding pure silica membrane calcined at a similar temperature, indicating the ability of the POSS to retain its porosity after pyrolysis. Subsequently, we investigated the influence of the norbornene (NB) functionality on the permeation properties of CMS membranes derived from a POSS–PI copolymer [14]. To the best of our knowledge, this is the only study on the permeation properties of a membrane derived from a carbonized POSS–PI (carbon-POSS) copolymer membrane. The POSS cage was functionalized with NB, yielding a POSS–PI composite with two improved

attributes: First, including NB helped increase the C/Si atomic ratio, which amplified the surface diffusion ability of the unpyrolyzed POSS–PI structure, thereby achieving a higher CO₂ permeance than that of the nonfunctionalized POSS–PI (6×10^{-9} and 2.5×10^{-9} mol m⁻² s⁻¹ Pa⁻¹, respectively) while retaining a CO₂/N₂ permeance ratio of 30. Second, the carbon-POSS membrane derived from the NB-functionalized POSS–PI retained the molecular sieving ability of the POSS–PI precursor membrane after heat treatment at 500 °C, in contrast to the nonfunctionalized POSS–PI. Heat-treating the NB-functionalized POSS–PI in an inert atmosphere induced crosslinking rather than decomposition in an oxidative atmosphere [14]. However, carbon-POSS membranes derived from POSS–PI composites require further scrutiny, for instance, to systematically evaluate their pyrolysis-temperature-dependent microstructural and permeation properties, which can broaden their applications.

In this study, the permeation behavior of carbon-POSS composite membranes was comprehensively examined by inspecting the role of NB functionalization of the POSS cage on the carbonization state. To this end, two POSS-PI precursors were selected: NB-functionalized POSS–polyimide–phenyl (POSS–PI–Ph–NB) and nonfunctionalized POSS–polyimide–phenyl (POSS–PI–Ph) (Figure 1). The effects of NB and its crosslinking (or lack thereof) on the pyrolytic properties and transformations of both precursors were studied. The pyrolysis-derived carbon-POSS materials were characterized to understand their structural transformations and post-pyrolysis carbonization states. Finally, the gas permeation properties and performance of the carbon-POSS membrane were evaluated, and its potential industrial applications were examined.

respectively. Tetraethoxysilane (TEOS) and zirconium *tert*-butoxide (ZrTB), which were also supplied by Sigma-Aldrich (Tokyo, Japan), were used to prepare a colloidal sol for fabricating the intermediate-layer membrane support.

2.2 Preparation of POSS–PI–Ph-, POSS–PI–Ph–NB-, and carbon-POSS-based gels, films, powders, and membranes

The POSS–PI–Ph–NB and POSS–PI–Ph synthesis procedures are detailed in Section S1 (Supplementary Information). To prepare solutions of the POSS–PI–Ph–NB and POSS–PI–Ph composites, the as-synthesized polymers were each dissolved in NMP at a concentration of 0.5 wt%, and the resulting mixtures were used to prepare films, xerogels, powders, and membranes. Notably, the POSS–PI–Ph–NB solution was prepared in two forms: with and without the DDB radical initiator (DDB/NB molar ratio of 0.01:1).

Each sample solution (100–150 μ L) was spin-coated onto UV-pretreated Si wafers and allowed to dry at 25–30 $^{\circ}$ C before calcination to prepare the films. The Si wafers coated with POSS–PI–Ph–NB and POSS–PI–Ph films were calcined in an inert atmosphere of flowing nitrogen at 200–800 $^{\circ}$ C to obtain carbon-POSS films. Xerogels of POSS–PI–Ph and POSS–PI–Ph–NB (with and without DDB) were formed by allowing their respective solutions to cure under slow drying conditions at 50–70 $^{\circ}$ C. Subsequently, carbon-POSS powder was obtained by calcination in nitrogen at the desired temperature.

Membranes were fabricated by first preparing the support layers, as described previously [28–30]. A typical α -Al₂O₃ tubular support sealed at one end (porosity: 60%; average pore size: 1.2 μ m; length: 10 cm; Nikkato Corporation, Japan) was coated with several layers of α -Al₂O₃ particles to further reduce the pore size to less than 100 nm and create a smoother surface. The

membrane support was eventually obtained after several layers of SiO₂-ZrO₂ colloidal sol were coated [28–31] until the pore size was reduced to within 1–2 nm. The successive support layers were fired in the air at 750 °C for 15–20 min. Active separation layers were subsequently formed by coating the POSS–PI–Ph–NB and POSS–PI–Ph solutions onto the prefabricated supports, followed by drying, curing, and calcination at the desired temperature in a nitrogen atmosphere for 30 min.

2.3 Characterization of gels, films, and powders

POSS–PI–Ph–NB- and POSS–PI–Ph-derived gels were prepared by drying the respective solutions at 50–70 °C to permit thermogravimetric analysis (TGA) in an N₂ atmosphere (DTG-60, Shimadzu, Japan). To that end, the sample was maintained at 100 °C for 2 h under N₂ flow (100 mL min⁻¹) to remove adsorbed water and then subjected to a temperature increase to 1000 °C at a ramping rate of 10 °C min⁻¹. The microtextural properties of the POSS–PI–Ph–NB and POSS–PI–Ph-derived powders were evaluated by acquiring N₂ adsorption–desorption isotherms at –196 °C using a BELMAX instrument (BELL, Japan). Before conducting these measurements, the powders were pretreated in a vacuum at 200 °C for 12 h to remove any pre-adsorbed gases, moisture, or vapor. Furthermore, the POSS–PI–Ph–NB-derived powders were subjected to attenuated total reflectance Fourier-transform infrared (ATR FT-IR) analysis at room temperature using an FT-IR spectrometer (FT/IR-4100, Jasco, Japan).

The transformations of the POSS and PI structures at different pyrolysis temperatures were investigated using ²⁹Si nuclear magnetic resonance (NMR) spectroscopy and X-ray photoelectron spectroscopy (XPS). Solid-state ²⁹Si magic angle spinning NMR spectra were recorded using an NMR spectrometer (Varian 600PS, Agilent, U.S.A.). XPS (Thermo-Fisher Scientific ESCALAB

250Xi, Al-Ka = 1486.6 eV) was conducted to analyze the change in the carbonization state by observing the shifts in the C 1s spectrum of the POSS–PI–Ph–NB-derived powders with pyrolysis temperature.

2.4 Evaluation of the permeation properties of the fabricated membranes

The process flow diagram of the gas permeation experimental rig devised in this study is shown in Figure S1. A single industrial-grade gas (He, H₂, CO₂, N₂, CH₄, CF₄, or SF₆) was fed to the exterior (upstream) of the membrane at a sufficiently high flow rate, whereas the permeate (downstream) was monitored by measuring the flow rate using a suitable flow meter (HORIBA-STECH; HORIBA, Japan). The permeation cell was maintained at a specific temperature between 50 and 200 °C to assess the temperature dependence of the permeation for each gas species. The permeance of each component was calculated by dividing the molar flow rate of the permeating gas by the product of the effective exterior surface area of the membrane and upstream and downstream pressure differences. Notably, the permeate-side flow rate was only recorded after a steady state was achieved.

The organic solvent dehydration properties of the carbon-POSS membranes were evaluated *via* pervaporation analysis. Details concerning the experimental pervaporation are provided in Section S2 (Supplementary Information), and a schematic of the pervaporation setup is shown in Figure S2.

3 Results and discussion

3.1 Effects of norbornene and its polymerization on the POSS–PI–Ph structure

The R groups surrounding the POSS cage feature two possible functionalities (Figure 1). In POSS–PI–Ph, the surrounding R groups comprised only PI–Ph units, accounting for 78% of the

total molecular weight, with the POSS cage accounting for the remaining 22%. The functionalization of POSS–PI–Ph with NB required some of the PI–Ph groups to be substituted with NB, which led to a reduction in the molecular weight ascribed to PI–Ph to 18%, whereas NB accounted for 60%, and POSS still retained 22% of its molecular weight. Figure 1 also shows two types of PI–Ph groups: a bridging PI–Ph that connects two POSS cages *via* a diphenoxy bridge and a terminating PI–Ph that freely occupies the POSS–PI–Ph ring. Therefore, the functionalization of POSS–PI–Ph with NB effectively demonstrated that substituting the terminating PI–Ph groups led to improved thermal stability [14]. Notably, the availability of substituted NB groups in the POSS–PI–Ph–NB ring presented an opportunity for their polymerization and thermal stability improvement.

The TGA of POSS–PI–Ph and POSS–PI–Ph–NB (with and without DDB) was conducted to evaluate their pyrolytic properties and gauge the success of NB polymerization in POSS–PI–Ph–NB. To this end, the TG curves of POSS–PI–Ph and POSS–PI–Ph–NB undergoing pyrolysis in an N₂ atmosphere were acquired (Figure 2). As mentioned earlier, the base POSS structure accounted for 22% of each hybrid by weight; this value was considered the limit of the residual weight for the pyrolyzed POSS–PI–Ph and POSS–PI–Ph–NB samples (black dashed line in Figure 2). Furthermore, the radical initiator DDB had a negligible contribution to the final residual weight (green profile in Figure 2) because its relative weight decreased abruptly to 0 at 200 °C. The onset of weight loss for POSS–PI–Ph occurred at a higher temperature than that for the POSS–PI–Ph–NB specimens with and without DDB. Comparing the final relative weights of all three samples indicated that adding DDB to POSS–PI–Ph–NB increased its relative residual weight to 0.6. Notably, the residual weights of all samples were higher than the weight content of the base POSS structure, indicating that the PI–Ph and NB decomposition products were present in the final

residue. Additionally, because the DDB/NB weight ratio was 0.02:1, the contribution of DDB decomposition to the early onset of weight loss was assumed to be negligible.

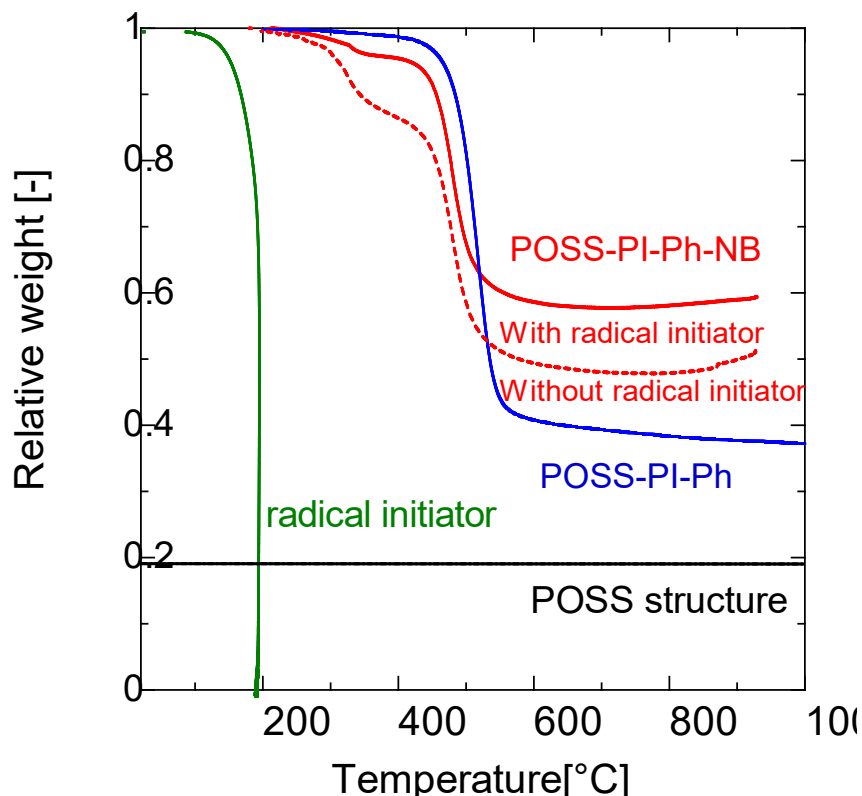


Fig. 2 TGA curves of different POSS-derived organic-inorganic composites.

As established above, carbon-POSS production with a high residual mass likely occurred through ring-opening metathesis polymerization (ROMP) of NB [32, 33]. According to a commonly reported mechanism governing the ROMP of NB (Figure 3), the resulting polynorbornene (PNB) also contains double bonds in its backbone and acts as a polykenamer that can be further vulcanized (or crosslinked) [33]. ROMP reactions traditionally proceed under the influence of transition metal chlorides; however, they are complex and hinder the production of polymers with controlled molecular weights [34]. Nevertheless, Boydston *et al.* demonstrated the

efficacy of metal-free catalysts for ROMP [35,36]. Therefore, DDB was used in this study as a metal-free radical initiator source. Notably, the early onset of weight loss for POSS-PI-Ph-NB (Figure 2) could be attributed to the retro or reversible Diels-Alder (rDA) reaction, in which the NB moieties decompose to form ethylene and cyclopentadiene upon exposure to higher temperatures [37,38]. Presumably, the catalyzed ROMP of NB occurred in conjunction with the rDA reaction at a faster rate, as the decomposition profile of POSS-PI-Ph-NB recovered shortly after the brief loss of NB-derived ethylene and cyclopentadiene. Faster recovery was observed in the presence of the DDB radical initiator, owing to the promotion of ROMP.

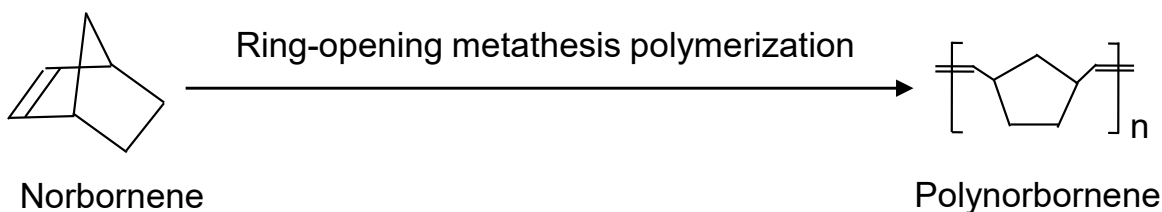


Fig. 3 Underlying mechanism for the ring-opening metathesis polymerization of NB.

The molecular size dependence of single-gas permeance was analyzed for the carbon-POSS membranes fabricated from POSS-PI-Ph and POSS-PI-Ph-NB at 200 °C (Figure 4). Both membranes were calcined at 700 °C to assess the contribution of PNB pyrolysis to the final membrane properties. The POSS-PI-Ph-NB sample used in this investigation was fabricated with DDB. Both membranes exhibited comparable He, H₂, and CO₂ permeance values of 4×10^{-6} , 6×10^{-6} , and $2.5 \times 10^{-6} \text{ mol m}^{-2} \text{ s}^{-1} \text{ Pa}^{-1}$, respectively, validating the production of highly permeable membranes (kinetic diameter: 0.26, 0.289, and 0.33 nm, respectively). However, the POSS-PI-Ph-NB-derived membrane showed superior rejection of larger-molecule gases such as CF₄ and SF₆ (kinetic diameter: 0.48 and 0.55 nm, respectively), and its H₂/CF₄ and H₂/SF₆ permeance ratios (333 and 857) were considerably higher than those of the POSS-PI-Ph-derived membrane (17 and

30). Although the ideal selectivity values of both membranes exceeded the Knudsen ratios, the higher values of the POSS–PI–Ph–NB-derived membrane indicate an enhancement in thermal stability due to the incorporation and polymerization of the NB moieties. Furthermore, the POSS–PI–Ph–NB-derived membrane exhibited a higher CH₄–CF₄ cutoff (kinetic diameters of 0.38 and 0.48 nm, respectively) than that of the POSS–PI–Ph-derived membrane, potentially indicating the existence of precise sieving channels with pore diameters of 0.48 nm or less. This can be attributed to the ultramicropores of the residual carbon produced after the pyrolysis of PNB. Therefore, the difference in the residual weights between POSS–PI–Ph–NB and POSS–PI–Ph in their TG profiles, which resulted from the substitution of certain PI–Ph moieties with NB, guided the carbon-POSS membrane to achieve precise molecular sieving.

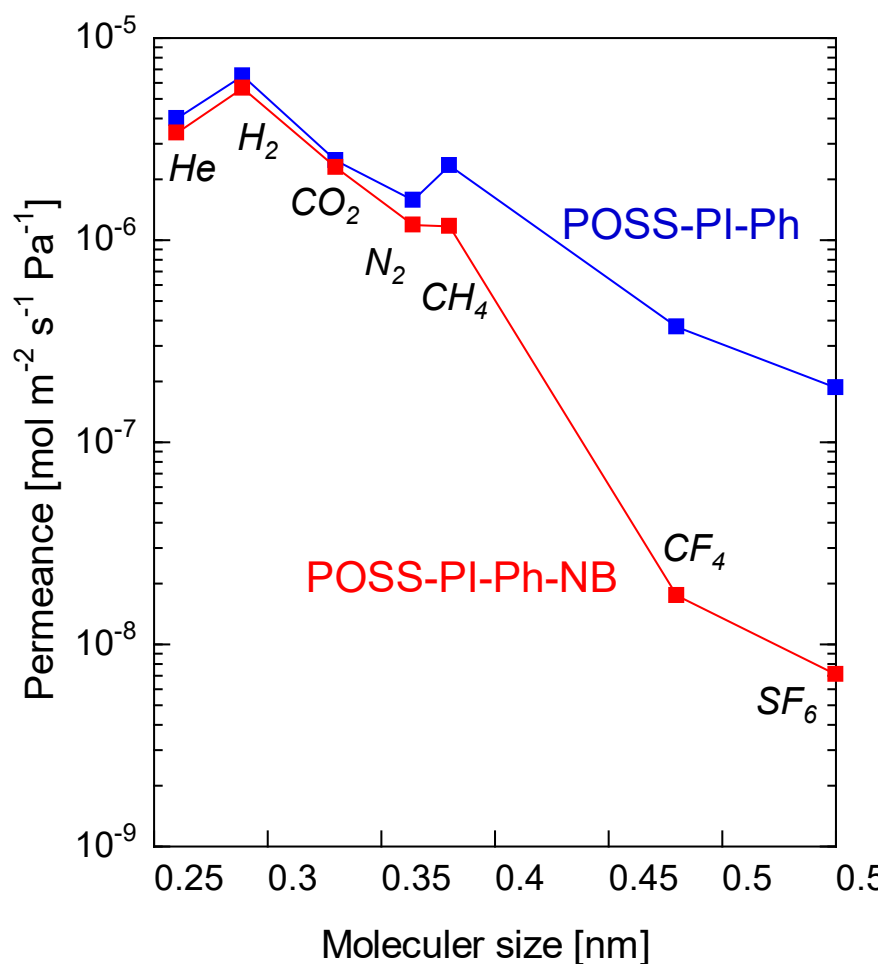


Fig. 4 Molecule size dependence of single-gas permeance measured at 200 °C for POSS–PI–Ph– and POSS–PI–Ph–NB-derived carbon-POSS membranes fabricated at 700 °C.

3.2 Characterization of the POSS–PI–Ph–NB-derived carbon-POSS structure

The positive effects of substituting terminal PI–Ph groups with NB on the thermal stability of POSS–PI–Ph–NB were clarified; however, analyzing the structural transformation of POSS–PI–Ph–NB during pyrolysis and characterizing the resulting carbon-POSS structure are crucial. As mentioned earlier (Figure 3), the pyrolysis of POSS–PI–Ph–PNB proceeds *via* simultaneous rDA and ROMP mechanisms, leading to a higher residual carbon content at 600–650 °C. Therefore, the transformation of the chemical structures of POSS–PI–Ph–PNB powders at different calcination temperatures was examined by ATR FT-IR analysis (Figure 5). The peaks appearing at 1,100–1,000 cm^{-1} for the powders calcined at 200 and 500 °C indicated an overlap between the siloxane bonds (Si–O–Si) of the POSS cage and Si–R bonds, signifying connections between the POSS cage, PI–Ph, and PNB. At the calcination temperatures mentioned above, the POSS cage was assumed to be largely connected to the PI–Ph and PNB polymer chains, given the appearance of the corresponding C–N, C=C, and C=O peaks attributed to the PI–Ph and PNB chains at 1,410, 1,600, and 1,700 cm^{-1} , respectively. However, they decreased slightly after calcination at 500 °C (Figure S3). After calcination at 600–800 °C, the aforementioned C–N, C=C, and C=O peaks no longer appeared owing to the pyrolysis of the PI–Ph and PNB chains. This finding is consistent with that of the TGA (Figure 3), in which the rapid decline in relative weight between 500 and 600 °C signaled the loss of the organic moieties. Concurrently, the peak at 1,100 cm^{-1} disappeared, revealing a peak representing the Si–O–Si bonds of the POSS cage at 1,000 cm^{-1} . Therefore, 500 °C represented the transition or commencement temperature for the pyrolytic conversion of POSS–PI–Ph–PNB to carbon-POSS, completed at 600–700 °C.

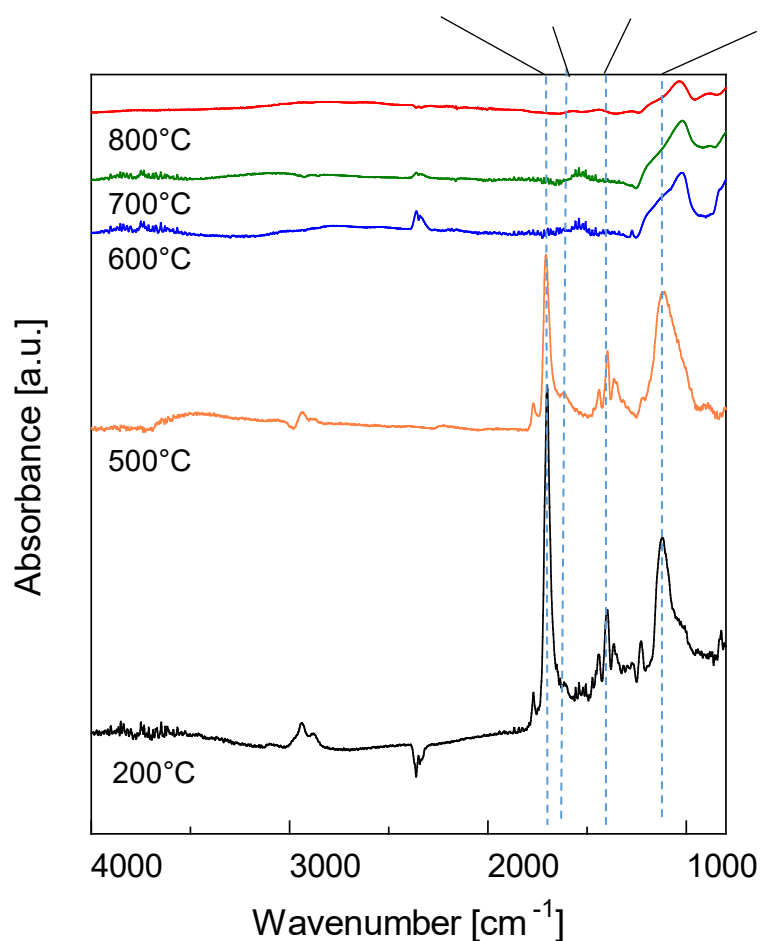


Fig. 5 FT-IR spectra of POSS-PI-Ph-PNB-derived films calcined at different temperatures.

The degree of transformation of PI-Ph and PNB into residual carbon and the POSS structure transformation at different calcination temperatures were analyzed using XPS and ^{29}Si solid-state NMR spectroscopy. Deconvoluted narrow C 1s spectra were acquired for the POSS-PI-Ph-PNB-derived samples calcined at 200, 500, and 700 °C (Figures 6a-c, respectively). The C 1s spectrum of POSS-PI-Ph-PNB calcined at 200 °C (Figure 6a) was deconvoluted into three peaks representing the different bonding states of carbon in the yet-to-be pyrolyzed copolymer: C-Si bonds, corresponding to links between the edge Si atoms of the POSS cage and the carbon atoms of the PI-Ph and PNB units; C=O/C-N bonds, representing the bonding of carbon to the

oxygen and nitrogen atoms in the PI-Ph and PNB units; and sp^3 C-C bonds, indicating the carbon-to-carbon bonds in the polymer chains. However, the obtained C 1s spectrum underwent notable changes after calcination at 500 °C (Figure 6b). First, the observed aggregate peak shifted to a lower binding energy from 285.9 to 285 eV. Furthermore, deconvolution of the aggregate peak suggested that the peak representing the C=O and C-N bonds disappeared, and the sp^3 C-C peak at 285.9 eV showed a significantly reduced intensity, giving way to a new sp^2 C-C peak at 284.8 eV. Therefore, the shift in the overall position of the narrow C 1s XPS peak after calcination at 500 °C was due to the formation of sp^2 C-C bonds owing to the polycondensation of the aromatic structures in PI-Ph and PNB [39,40]. The acquired spectra remained largely the same after calcination at 700 °C (Figure 6c), with only a slight increase in the intensity observed for the sp^2 C-C peak. Notably, along with the sp^2 C-C peak, the sp^3 C-C and C-Si peaks remained noticeable in the deconvoluted spectrum after calcination at 700 °C.

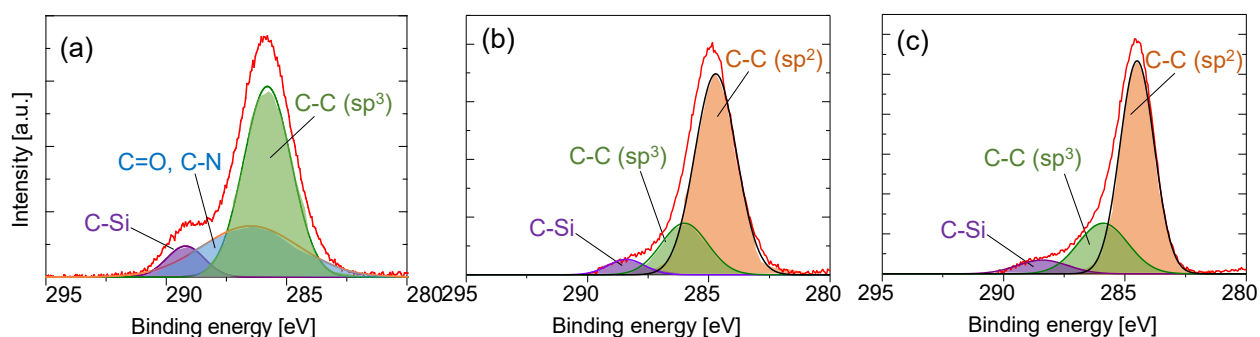


Fig. 6 XPS profiles of POSS-PI-Ph-PNB-derived samples prepared at (a) 200, (b) 500, and (c) 700 °C.

To further confirm the state of bonding in the POSS silica structure in relation to the PI-Ph and PNB units during pyrolysis, ^{29}Si solid-state NMR spectra were acquired for the POSS-PI-Ph-PNB-derived powders calcined at 200 and 700 °C (Figures 7a and b, respectively). The

observed peaks were typical of Si bonds [41]. For the powder calcined at 200 °C (Figure 7a), the peak appearing at -66.7 ppm was designated as T₃, which represented O₃SiC bonds (see inset). This finding corroborated the presumption that the POSS cage remained connected to carbon atoms in the PI-Ph and PNB units. After calcination at 700 °C (Figure 7b), intense overlapping peaks denoted as Q₄ and Q₃ appeared at -110.1 and -101.6 ppm, respectively. Q₄ represents SiO₄ bonds, indicating the conversion of Si-C bonds to Si-O bonds during the pyrolysis of PI-Ph and PNB. The Si-O bonds were presumably established by the oxidation of free Si radicals formed after the cleavage of the Si-C bonds. During pyrolysis, oxygen radicals were assumed to be produced *via* the decomposition of PI-Ph and PNB, resulting in a possible oxidation reaction between the Si and O radicals. Q₃ represents the unexpected formation of Si-OH bonds, which is likely due to moisture adsorbed onto the silica structure. Importantly, despite the high calcination temperature of 700 °C, the T₃ peak representing O₃SiC persisted at -64.1 ppm. This finding substantiates the XPS results that highlighted the persistence of the Si-C peaks after calcination at 700 °C.

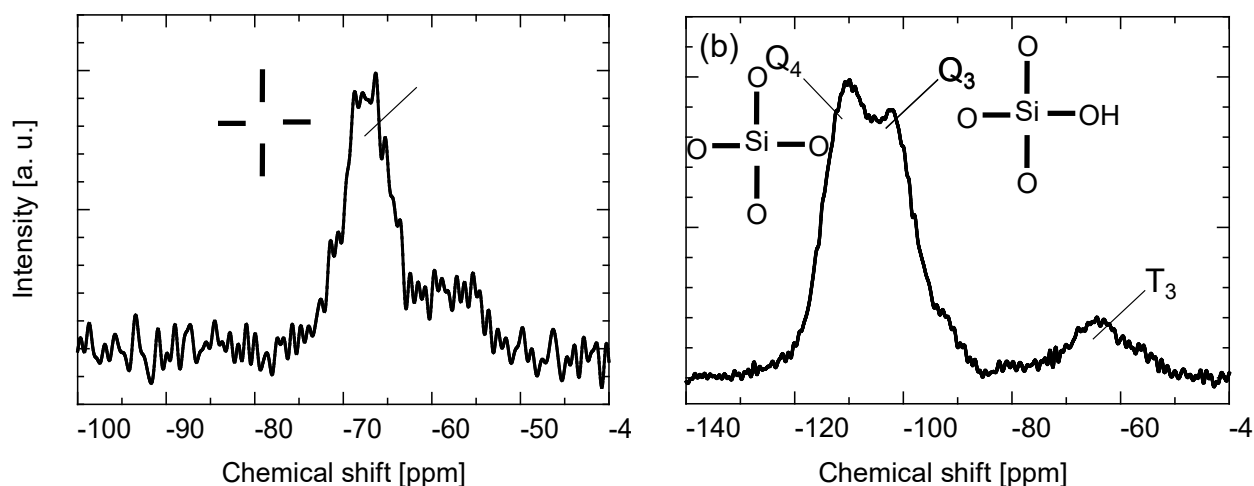


Fig. 7 ²⁹Si-NMR spectra of POSS-PI-Ph-PNB-derived samples prepared at (a) 200 and (b) 700 °C.

The structural transformation during the pyrolysis of POSS–PI–Ph–PNB to carbon-POSS (Figure 8) was then analyzed based on the inferences from the results shown in Figures 6 and 7. The POSS cage was assumed to be connected to the residual carbon structures *via* Si–C bonds, and the sp^2 -hybridized carbon was assumed to still feature sp^3 defects (Figure 6c), which potentially served as permeation pathways for hydrogen and other similar small molecules [42]. Therefore, analogous structures of CMSs featuring molecule-sieving ultramicropores of sp^2 carbon and structurally intact POSS cages were obtained, which led to the carbon-POSS membranes exhibiting higher permselectivity than that of conventional CMS membranes.

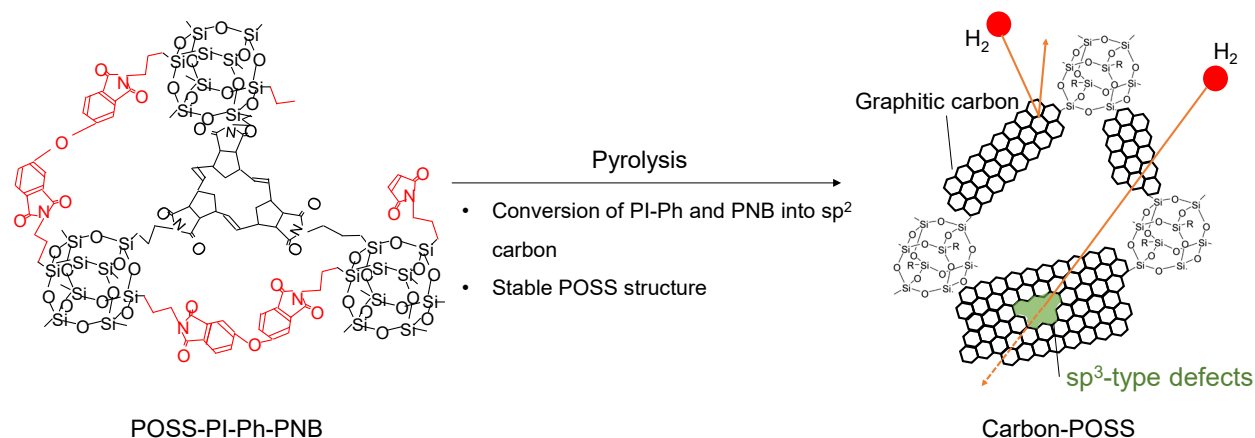


Fig. 8 Schematic illustrating the pyrolytic conversion of POSS–PI–Ph–PNB to carbon-POSS

3.3 Gas permeation properties and performance of carbon-POSS membranes

3.3.1 Effects of pyrolysis temperature on membrane properties

The gas permeation properties of membranes based on POSS–PI–Ph–PNB fabricated at different calcination temperatures were evaluated to analyze the microstructural evolution of the membrane and its subsequent effects on the separation potential. To this end, the permeance of single gases (H_2 , He, CO_2 , N_2 , CH_4 , CF_4 , and SF_6) and the ideal He/ SF_6 , He/ N_2 , and N_2/SF_6 selectivities at 200 °C were examined with respect to the membrane calcination temperature

(Figure 9a). As established in the preceding section, the POSS–PI–Ph–PNB structure remained largely intact at a calcination temperature of 200 °C. Therefore, the hybrid polymer exhibited dense POSS, PI–Ph, and PNB polymer microstructures, resulting in low gas permeances but high ideal He/SF₆ and N₂/SF₆ selectivities of 9,000 and 300, respectively. The permeance of all investigated gases followed a similar trend with increasing calcination temperatures. The permeance of the large-molecule gases (CF₄ and SF₆; kinetic diameters \geq 0.48 nm) reached a maximum for the membrane calcined at 600 °C, whereas the permeance of the small-molecule gases (H₂, He, CO₂, N₂, and CH₄; kinetic diameters \leq 0.38 nm) did so at 700 °C. The increase in gas permeance between 200 and 600 °C was evidently related to the initial decomposition of the organic moieties of the PI–Ph and PNB units that served as pore-generating templates. At 700 °C, when the small-molecule gases achieved maximum permeance values, CF₄ and SF₆ showed a decreasing tendency, indicating higher selectivity for small-molecule gases over large-molecule ones. This suggests that the generation of pores with diameters smaller than 0.48 nm was vital to rejecting molecules with sizes larger than this value.

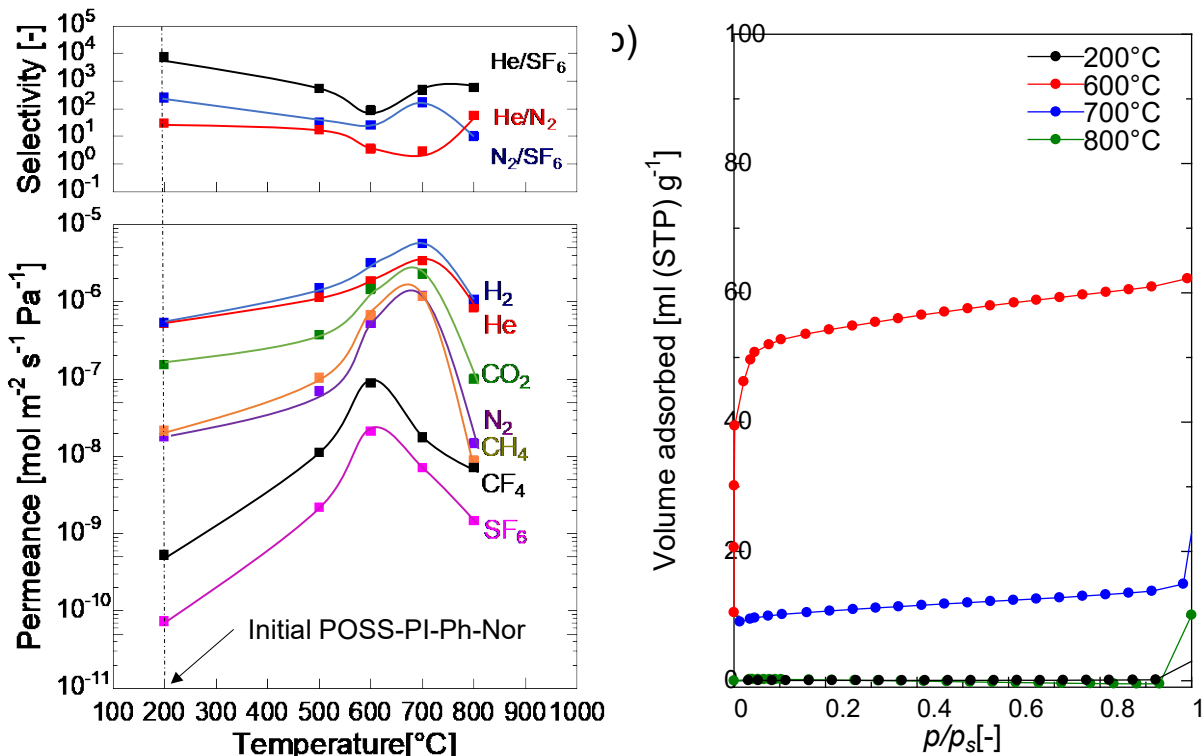


Fig. 9 (a) Dependence of single-gas permeance and permeance ratios at 200 °C on the temperature at which the POSS-PI-Ph-PNB membrane was pyrolyzed. (b) N_2 adsorption isotherms of POSS-PI-Ph-PNB-derived powders calcined at different temperatures.

The molecule-sieving pores were generated, presumably owing to the sp^2 residual carbon and the production of more Si-O bonds (Figures 7a and b). Upon further calcination at 800 °C, all the gas permeance and ideal selectivity values decreased owing to the continuation of thermally induced structural densification. This trend was corroborated by the N_2 adsorption isotherms acquired at -196 °C for bulk samples calcined at 200–800 °C (Figure 9b). POSS-PI-Ph-PNB calcined at 200 °C had an extremely low amount of adsorbed N_2 , substantiating the presence of a dense copolymer structure. However, the amount of adsorbed N_2 increased as the calcination temperature was increased to 600 °C, owing to the opening of new pores caused by the decomposition of PI-Ph and PNB. Increasing the pyrolysis temperature to 700 and 800 °C led to

a reduced amount of N_2 adsorbed and an eventual dense state, respectively. Therefore, a calcination temperature of 700 °C was considered optimal for yielding carbon-POSS membranes with remarkable molecular sieving performance. Figures 10a and b show the cross-sectional morphologies of POSS–PI–Ph–PNB and POSS–PI–Ph–PNB-derived carbon-POSS membranes fabricated at 200 and 700 °C, respectively. The thickness of the POSS–PI–Ph–PNB layer on the SiO_2 – ZrO_2 / Al_2O_3 support layers was estimated to be 30 nm. However, after conversion to a carbon-POSS composite membrane at 700 °C, the thickness decreased to 5 nm, indicating 83% shrinkage due to the pyrolytic conversion. This corresponds to the weight loss observed in the thermogravimetric analysis of the POSS–PI–Ph–PNB sample (Figure 2).

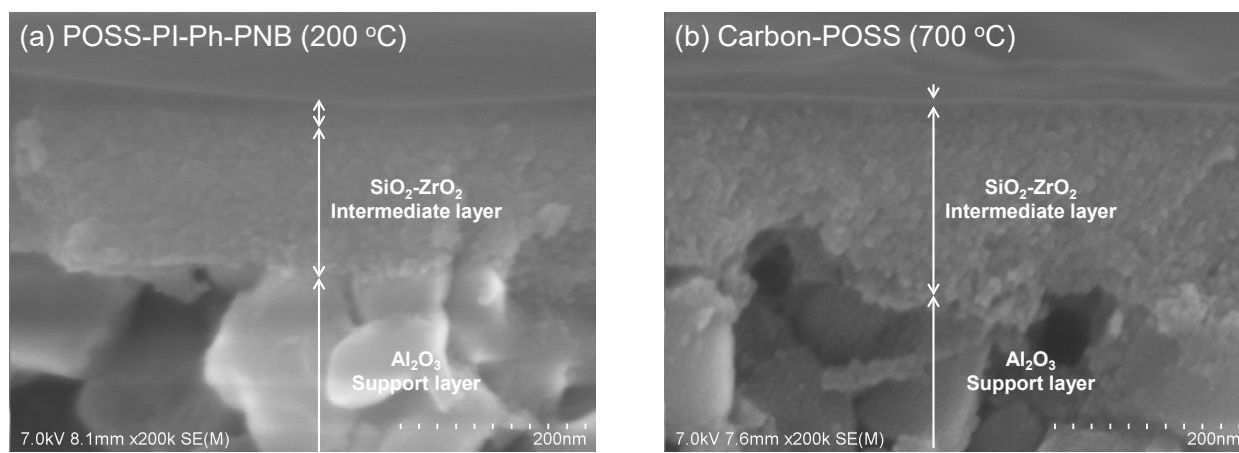


Fig. 10 Cross-sectional morphologies of POSS–PI–Ph–PNB and POSS–PI–Ph–PNB-derived carbon-POSS membranes fabricated at 200 and 700 °C, respectively.

The microstructural effects of the pyrolysis temperature on the carbon-POSS membranes were further analyzed by examining the temperature dependence of gas permeance (Figure 11a). To that end, the He permeance of POSS–PI–Ph–PNB-derived carbon-POSS membranes was investigated at different temperatures between 50 and 200 °C. The experimental data were fitted to Equation 1, which was derived from the modified gas translational model proposed by Lee *et*

al. [43] and Nagasawa *et al.* [44]. In Equation 1, P is the permeance of the permeating species, k_0 is the pre-exponential factor associated with the membrane configuration, M is the molecular weight of the permeating gas, R is the gas constant, T is the absolute temperature, and E_p is the permeation activation energy. He exhibited an activated-diffusion-type permeation mechanism for all membranes, in which its permeance increased with increasing permeation temperature. According to gas permeation models, gas molecules percolating through activated diffusion require sufficient energy to overcome the potential energy barriers within the micropores [45]. This energy, denoted as E_p , can be calculated using Equation 1, given as:

$$P = \frac{k_0}{\sqrt{MRT}} \exp\left(-\frac{E_{p,i}}{RT}\right) \quad (1)$$

A plot of the E_p values of He as a function of the membrane calcination temperature (Figure 11b) clearly revealed a dependence between the activation energy of He permeation through the POSS–PI–Ph–PNB-derived membranes and the calcination temperature. E_p initially decreased from 18.1 kJ/mol at a calcination temperature of 200 °C to 12.6 kJ/mol at 700 °C before increasing abruptly to 17.8 kJ/mol at 800 °C. The initial decrease in the E_p value of He correlates with the increased He permeance as the calcination temperature increases from 200 to 700 °C, signifying a reduction in the potential energy barrier in the membrane pores and a consequent increase in the pore size. Therefore, at 700 °C, decomposition of the PI–Ph and PNB units combined with the generation of molecule-sieving residual carbon channels and more compact Si–O–Si linkages created free volumes in the pores, which were sufficiently large to allow permeation of small- and mid-sized molecules but small enough to reject larger molecules.

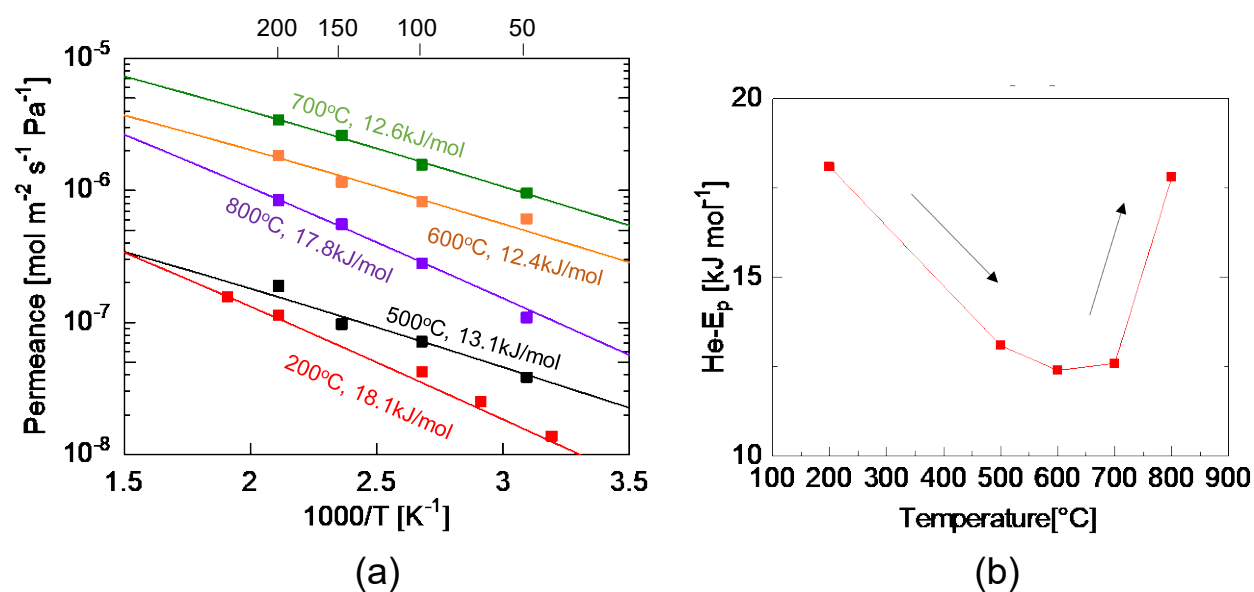


Fig. 11 (a) Temperature dependence of He permeance for the POSS-PI-Ph-PNB-derived membranes. (b) Effects of pyrolysis temperature on the He activation energy (He-E_p).

3.3.2 Performance of carbon-POSS in relation to state-of-the-art membranes

In this study, the presence of a rigid POSS cage in a CMS network was considered to alleviate one of the drawbacks of CMS membranes: achieving high selectivity with low permeance because the carbon-POSS membranes were expected to simultaneously exhibit high permeance and high selectivity. A comparison with the literature suggests that carbon-POSS membranes exhibit considerably higher permeance values than state-of-the-art CMS membranes. Essentially, the tradeoff between H_2/N_2 selectivity and H_2 permeance was compared for the selected polymer-derived CMS membranes and the carbon-POSS membranes developed in this study (Figure 12; see Table 1 for more details). The comparison indicates that polymer-derived CMS membranes generally exhibit low permeances (even for hydrogen) but significantly high selectivities, irrespective of the polymer precursor. Notably, the ultramicroporous structure and tight stacking of graphitic carbon sheets in CMSs, which allow intense molecular sieving between small-sized

gases, also prevent them from achieving high gas permeance. Furthermore, although previously reported CMS membranes were fabricated at different temperatures, they exhibited similar behaviors in terms of the aforementioned tradeoff. In contrast, the carbon-POSS membranes exhibited considerably higher hydrogen permeances than those of many CMS membranes (Figure 12); however, they also showed lower H_2/N_2 selectivities owing to the simultaneous high permeation of H_2 and N_2 caused by the preservation of their porous structure even after pyrolysis of the precursor at 700 °C.

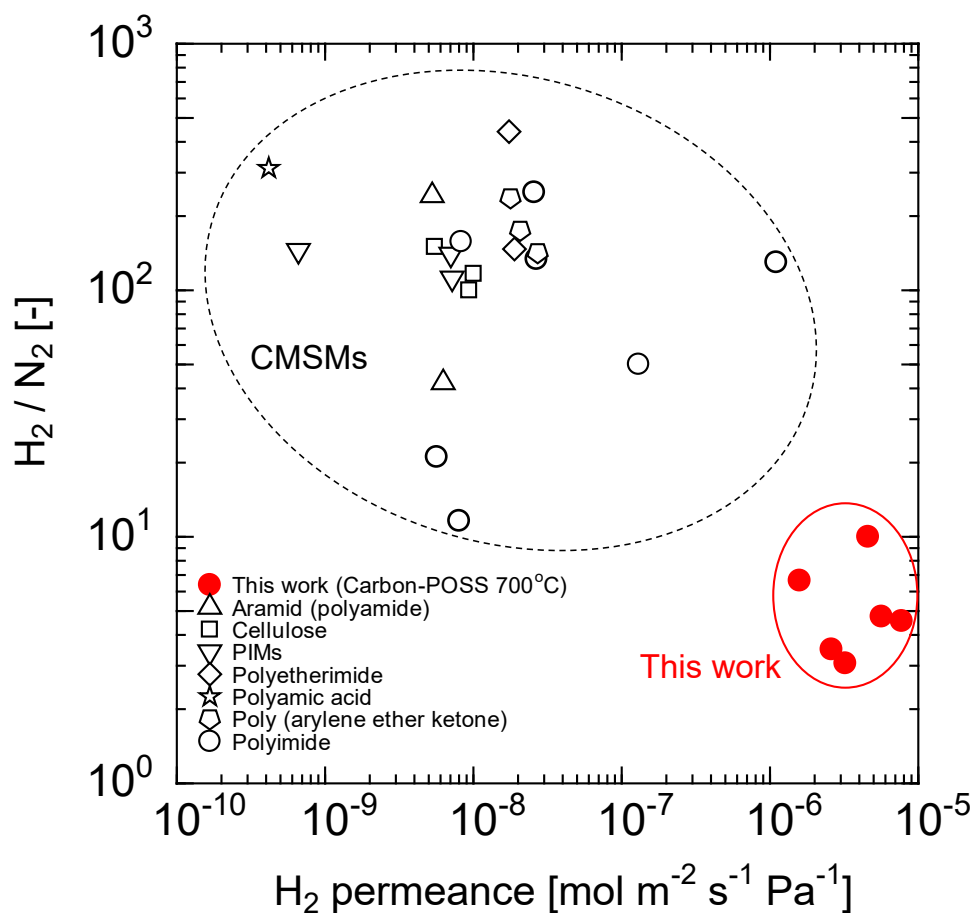


Fig. 12 Tradeoff comparison between the H_2/N_2 selectivity and H_2 permeance for various polymer-derived carbon molecular sieve (CMS) membranes and the carbon-POSS membranes fabricated in this study.

421 Table 1 Properties and performance of state-of-the-art polymer-derived CMS membranes
 422 compared with those of the carbon-POSS membranes

Membrane precursor	Pyrolysis temperature [°C]	H ₂ permeability [Barrer]	H ₂ permeance [10 ⁻⁷ mol m ⁻² s ⁻¹ Pa ⁻¹]	$\alpha_{\text{H}_2/\text{N}_2}$ [-]	Reference
Aramid (polyamide)	800	86.2	0.007	1486.2	[46]
	550	747.2	0.063	42.2	[46]
	675	629.7	0.053	242.2	[46]
Cellulose	550	300	0.055	150	[47]
	550	600	0.094	100	[47]
	550	700	0.100	116.7	[47]
Brominated PIM	350	1503	0.072	112	[48]
	350	1472	0.007	145	[48]
	350	138	0.070	140	[48]
PEI	600	3838	0.189	147	[49]
	600	3531	0.174	440	[49]
PAA	700	84.4	0.0042	312.6	[50]
PEK	700	5262	0.271	142	[51]
	800	3701	0.207	175	[51]
	900	2919	0.178	237	[51]
Polyimide	550	7462	1.298	50.16	[52]

	600	1231	0.082	157.6	[52]
	700	-	11.0	130	[42]
	700	2300	0.257	250	[53]
Carbon- POSS	700	-	76.8	4.65	Present study
	700	-	54.3	4.77	Present study
	700	-	44.6	10.17	Present study

α : Ideal selectivity; PIM: polymer of intrinsic microporosity; PEI: polyetherimide, PAA: polyamic acid; PEK: poly(arylene ether ketone).

As discussed previously, the carbon-POSS membranes prepared at 700 °C exhibited maximum permeance for gases with kinetic diameters ≤ 0.38 nm (H_2 , He, CO_2 , N_2 , and CH_4) but showed a declining trend for gases with kinetic diameters ≥ 0.48 nm (CF_4 and SF_6) (Figure 9), indicating that the generation of pores less than 0.48 nm in size was crucial for impeding large molecules. Therefore, carbon-POSS membranes that could adequately separate molecules with kinetic diameters of 0.26–0.55 nm were viably fabricated. Notably, the carbon-POSS membrane obtained at a pyrolysis temperature of 700 °C achieved high selectivity and permeance.

Membranes with decent separation abilities for molecules with diameters in the aforementioned range are currently gaining attention. In this study, ideal N_2/SF_6 separation (kinetic diameters of N_2 and SF_6 : 0.364 and 0.55 nm, respectively) was adopted as an indicator to assess the performance of the carbon-POSS membrane calcined at 700 °C. A tradeoff plot was constructed to compare the performance of the carbon-POSS membranes fabricated at different

temperatures (200–800 °C) to that of previously reported membranes such as those containing organosilica [54,55], aminosilica [56], zeolites [57–63], and polymers [64–66] (Figure 13; see Table S1 for more details). The results suggest that the carbon-POSS membranes fabricated at 700 °C surpass their counterparts fabricated at other temperatures and compete favorably with state-of-the-art membranes while exhibiting reproducible N_2 permeance and ideal N_2/SF_6 selectivity values of $10^{-6} \text{ mol m}^{-2} \text{ s}^{-1} \text{ Pa}^{-1}$ and 100–200, respectively.

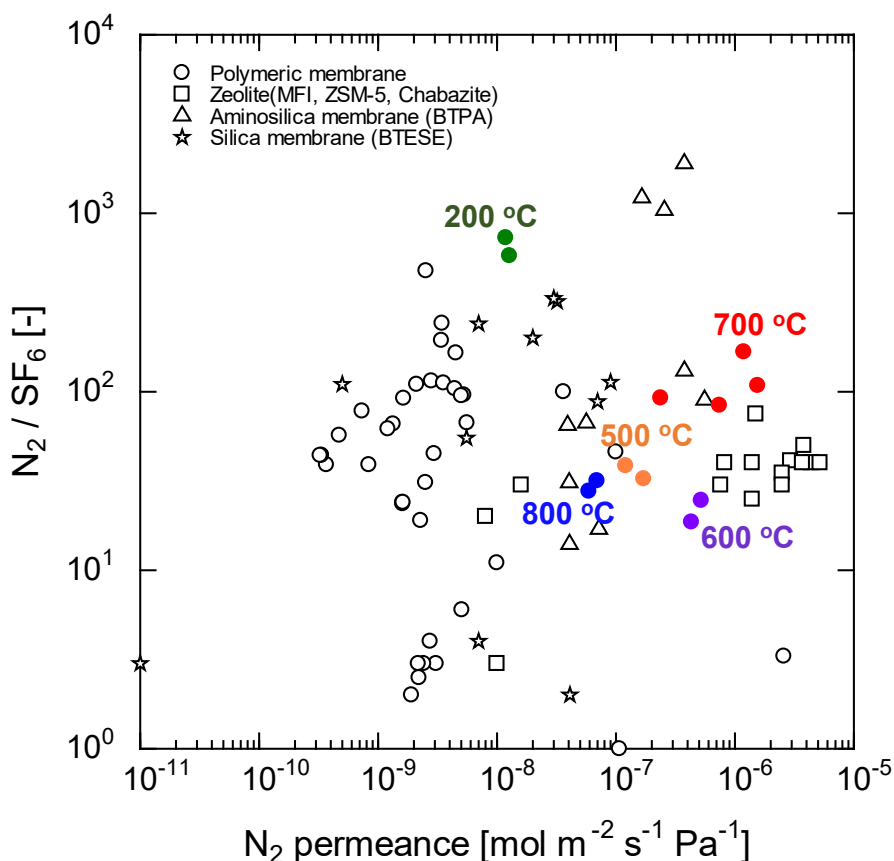


Fig. 13 Tradeoff between N_2 permeance and the N_2/SF_6 permeance ratio investigated for the carbon-POSS membranes and other membrane types such as organosilica [54,55], aminosilica [56], zeolites [57–63], and polymers [64–66].

4 Outlook

This report highlights the feasibility of using carbon-POSS membranes to separate molecules with kinetic diameters between 0.26 and 0.55 nm. Because carbon-POSS membranes exhibit ideal performance compared to other membrane types (Figure 13), they show promise for applications such as the recovery of SF₆ from N₂. Additionally, these membranes can potentially exhibit decent performance for separating other similarly-sized molecules such as propylene and propane (kinetic diameter/Lennard-Jones length constant: 0.45/0.506 nm and 0.43/0.46 nm, respectively) and pervaporation dehydration of organic solvents such as methanol, ethanol, isopropyl alcohol, and *tert*-butanol (kinetic diameter: 0.38, 0.43, 0.47, and 0.51 nm, respectively). Notably, the carbon-POSS membranes showed promising results for the initial dehydration of methanol, ethanol, and isopropyl alcohol in time-course experiments (Figure S4). Further, this experiment showed no water flux or permeance loss during pervaporation dehydration, suggesting resistance to the physical aging phenomenon associated with pure carbon molecular sieve membranes. Thus, long-term maintenance of high separation performance is expected for carbon-POSS membranes. Future investigations will help extend the understanding and applications of the developed membranes to other organic solvents.

Tuning the carbon-POSS membrane properties further can be attempted by tweaking the respective proportions of PI-Ph, NB, and POSS. In this study, a predetermined composition (as supplied) and several contributing factors were used to construct the carbon-POSS structures and membranes. Future studies will target the fabrication of membranes with different separation properties and applications by utilizing different amounts of hybrid POSS-PI-Ph-NB copolymer components.

5 Conclusions

To the best of our knowledge, this is the first report on polynorbornene (PNB) vulcanization of a polyhedral oligomeric silsesquioxane (POSS) to create a carbonized POSS structure, focusing on clarifying the role of this structure in determining the gas permeation mechanism. NB substituted 60% of the Ph-PI units in the POSS-PI-Ph structure. Using 2,3-dimethyl-2,3-diphenyl butane as a radical initiator promoted the metal-free crosslinking of NB and subsequent vulcanization to achieve a high residual carbon content. The pyrolysis of POSS-PI-Ph-PNB yielded a stable carbonized structure with sp^2 -hybridized carbons connected to the POSS cage.

The carbon-POSS membranes exhibited enhanced permeances for several gases with increasing precursor pyrolysis temperature. Notably, early onset of the reduction in permeance for large-molecule gases such as CF_4 and SF_6 after 600 °C ensured that a high N_2 permeance and ideal N_2/SF_6 selectivity exceeding $10^{-6} \text{ mol m}^{-2} \text{ s}^{-1} \text{ Pa}^{-1}$ and 100, respectively, could be achieved using the membrane fabricated from POSS-PI-Ph-NB at 700 °C; this finding underscores the promise of the membrane for separating N_2 and SF_6 ; paraffins and olefins; and organic solvent mixtures through pervaporation dehydration. Overall, high-performance carbonized POSS-derived membranes can be fabricated by optimizing the NB functionality and POSS content of the hybrid copolymer precursor.

491 ASSOCIATED CONTENT

492 **Supporting information**

493 Section S1. Synthesis of POSS–PI–Ph–NB and POSS–PI–Ph.

494 Section S2. Evaluation of the pervaporation (PV) dehydration performance of carbon-POSS
495 membranes.

496 Fig. S1 Flow diagram of the gas permeation setup and the corresponding operating conditions.

497 Fig. S2 Flow diagram of the experimental setup adopted for pervaporation analysis.

498 Fig. S3 Normalized absorbance values of the C=O- and C–N-related FT-IR spectral peaks shown
499 in Figure 5.

500 Fig. S4 Long-term PV performance of a carbon-POSS membrane in different H₂O/organic
501 solvent systems.

502 Table S1 Ideal N₂/SF₆ separation performance of different state-of-the-art membranes and the
503 carbon-POSS membrane developed in this study.

504 This information is available free of charge via the Internet at <http://pubs.acs.org/>.

505 AUTHOR INFORMATION

506 **Corresponding author**

507 **Masakoto Kanezashi**

508 Chemical Engineering Program, Graduate School of Advanced Science and Engineering,
509 Hiroshima University, 1-4-1 Kagamiyama, Higashi-Hiroshima 739-8527, Japan

510 **E-mail address:** kanezashi@hiroshima-u.ac.jp

511 **Author contributions**

512 S. O. L.: investigation, data curation, writing (original draft preparation); K. W.: investigation,
513 data curation; R. U.: data curation; N. M.: supervision; H. N.: supervision, writing (editing and
514 revision); T. T.: supervision, validation, writing (editing and revision); M. K.: conceptualization,
515 methodology, writing (original draft preparation and revision), funding acquisition.

516 **Conflicts of interest**

517 The authors declare no conflicts of interest.

518

519

520

521

522

523

524

525

526

527

528

529

530

531

532

533

534

References

1. Baney, R. H.; Itoh, M.; Sakakibara, A.; Suzuki, T. Silsesquioxanes. *Chem. Rev.* **1995**, *95*, 1409–1430.
2. Li, G.; Wang, L.; Ni, H.; Pittman Jr., C. U. Polyhedral Oligomeric Silsesquioxane (POSS) Polymers and Copolymers: A Review. *J. Inorg. Organomet. Polym.* **2001**, *11*, 123–154.
3. Zhou, H.; Ye, Q.; Xu, J. Polyhedral Oligomeric Silsesquioxane-Based Hybrid Materials and Their Applications. *Mater. Chem. Front.* **2017**, *1*, 212.
4. Zhang, W.; Camino, G.; Yang, R. Polymer/Polyhedral Oligomeric Silsesquioxane (POSS) Nanocomposites: An Overview of Fire Retardance. *Prog. Polym. Sci.* **2017**, *67*, 77–125.
5. Mohamed, M. G.; Kuo, S. W. Functional Silica and Carbon Nanocomposites Based on Polybenzoxazines. *Macromol. Chem. Phys.* **2019**, *220*, 1800306.
6. Muhammad, S.; Niazi, J. H.; Shawuti, S.; Qureshi, A. Functional POSS Based Polyimide Nanocomposite for Enhanced Structural, Thermal, Antifouling and Antibacterial Properties. *Mater. Today Commun.* **2022**, *31*, 103287.
7. Wang, J.; Ruofan, R.; Liu, R.; Ping, A.; Wang, Z.; Liu, J.; Zhang, S.; Liu, Y. DC Surface Flashover Characteristics of Polyimide Containing Polyhedral Oligomeric Silsesquioxane (POSS) in the Main Chains under Vacuum. *Polymers* **2022**, *14*, 2453.
8. Kim, Y.; Choi, J. Thermal Ablation Mechanism of Polyimide Reinforced with POSS under Atomic Oxygen Bombardment. *Appl. Surf. Sci.* **2021**, *561*, 150578.
9. Qian, M.; Mao, X.; Wu, M.; Cao, Z.; Liu, Q.; Sun, L.; Gao, Y.; Xuan, X.; Pan, Y.; Niu, Y.; Gong, S. POSS Polyimide Sealed Flexible Triple-Junction GaAs Thin-Film Solar Cells for Space Applications. *Adv. Mater. Technol.* **2021**, *6*, 2100603.

- 558 10. Qian, M.; Zhou, B.; Liu, G.; Gao, Y.; Niu, Y.; Gong, S. Polyhedral Oligomeric Silsesquioxane
559 Polyimide Nanocomposites for Color Filters and Flexible Conductive Films. *J. Appl. Polym. Sci.* **2021**, *138*, e50372.
- 561 11. Dasgupta, B.; Sen, S. K.; Banerjee, S. Aminoethyl Aminopropylisobutyl POSS—Polyimide
562 Nanocomposite Membranes and Their Gas Transport Properties. *Mater. Sci. Eng. B* **2010**, *168*,
563 30–35.
- 564 12. Le, N. L.; Chung, T.-S. High-Performance Sulfonated Polyimide/Polyimide/Polyhedral
565 Oligosilsesquioxane Hybrid Membranes for Ethanol Dehydration Applications. *J. Membr. Sci.*
566 **2014**, *454*, 62–73.
- 567 13. Iyer, P.; Iyer, G.; Coleman, M. Gas Transport Properties of Polyimide–POSS Nanocomposites.
568 *J. Membr. Sci.* **2010**, *358*, 26–32.
- 569 14. Kanezashi, M.; Tomarino, Y.; Nagasawa, H.; Tsuru, T. Tailoring the Molecular Sieving
570 Properties and Thermal Stability of Carbonized Membranes Containing Polyhedral Oligomeric
571 Silsesquioxane (POSS)-Polyimide via the Introduction of Norbornene. *J. Membr. Sci.* **2019**,
572 *582*, 59–69.
- 573 15. Burns, G. T.; Taylor, R. B.; Xu, Y.; Zangvil, A.; Zank, G. A. High-Temperature Chemistry of
574 the Conversion of Siloxanes to Silicon Carbide. *Chem. Mater.* **1992**, *4*, 1313–1323.
- 575 16. Xiao, Y.; Lei, X.; Liu, Y.; Zhang, Y.; Ma, X.; Zhang, Q. Double-Decker-Shaped Phenyl-
576 Substituted Silsesquioxane (DDSQ)-Based Nanocomposite Polyimide Membranes with
577 Tunable Gas Permeability and Good Aging Resistance. *Sep. Purif. Technol.* **2023**, *315*, 123725.
- 578 17. Rau, A. V.; Knott, K.; Lu, K. Porous SiOC/SiC Ceramics via an Active-Filler-Catalyzed
579 Polymer-Derived Method. *Mater. Chem. Front.* **2021**, *5*, 6530.

- 580 18. Hazazi, K.; Ma, X.; Wang, Y.; Ogieglo, W.; Alhazmi, A.; Han, Y.; Pinnau, I. Ultra-Selective
581 Carbon Molecular Sieve Membranes for Natural Gas Separations based on a Carbon-Rich
582 Intrinsically Microporous Polyimide Precursor. *J. Membr. Sci.* **2019**, *585*, 1–9.
- 583 19. Hou, M.; Qi, W.; Li, L.; Xu, R.; Xue, J.; Zhang, Y.; Song, C.; Wang, T. Carbon Molecular
584 Sieve Membrane with Tunable Microstructure for CO₂ Separation: Effect of Multiscale
585 Structures of Polyimide Precursors. *J. Membr. Sci.* **2021**, *635*, 119541.
- 586 20. Xu, S.; Zhao, N.; Wu, L.; Kang, S.; Zhang, Z.; Huo, G.; Dai, Z.; Li, N. Carbon Molecular Sieve
587 Gas Separation Membranes from Crosslinkable Bromomethylated 6FDA-DAM Polyimide. *J.*
588 *Membr. Sci.* **2022**, *659*, 120781.
- 589 21. Hou, M.; Li, L.; Song, J.; Xu, R.; He, Z.; Lu, Y.; Pan, Z.; Song, C.; Wang, T. Polyimide-
590 Derived Carbon Molecular Sieve Membranes for High-Efficient Hydrogen Purification: The
591 Development of a Novel Phthalide-Containing Polyimide Precursor. *Sep. Purif. Technol.* **2022**,
592 *301*, 121982.
- 593 22. Liu, G.; Li, R.; Chen, X.; Cheng, L.; Liu, Y.; Liu, G.; Jin, W. Pyrolysis Temperature-Regulated
594 Gas Transport and Aging Properties in 6FDA-DAM Polyimide-Derived Carbon Molecular
595 Sieve Membranes. *Sep. Purif. Technol.* **2023**, *313*, 123459.
- 596 23. Karunaweera, C.; Musselman, I. H.; Balkus Jr., K. J.; Ferraris, J. P. Fabrication and
597 Characterization of Aging Resistant Carbon Molecular Sieve Membranes for C₃ Separation
598 Using High Molecular Weight Crosslinkable Polyimide, 6FDA-DABA. *J. Membr. Sci.* **2019**,
599 *581*, 430–438.
- 600 24. Liu, Z.; Qiu, W.; Quan, W.; Koros, W. J. Advanced Carbon Molecular Sieve Membranes
601 Derived from Molecularly Engineered Cross-Linkable Copolyimide for Gas Separations. *Nat.*
602 *Mater.* **2023**, *22*, 109–116.

25. Liu, Z.; Qiu, W.; Koros, W. J. New Insights into Physical Aging-Induced Structure Evolution in Carbon Molecular Sieve Membranes. *Angew. Chem. Int. Ed.* **2022**, *61*, e202210831.
26. Hays, S. S.; Sanyal, O.; Leon, N. E.; Arab, P.; Koros, W. J. Envisioned Role of Slit Bypass Pores in Physical Aging of Carbon Molecular Sieve Membranes, *Carbon* **2020**, *157*, 385–394
27. Kanezashi, M.; Shioda, T.; Gunji, T.; Tsuru, T. Gas Permeation Properties of Silica Membranes with Uniform Pore Sizes Derived from Polyhedral Oligomeric Silsesquioxane. *AIChE J.* **2012**, *58*, 1733–1743.
28. Lawal, S.; Kanezashi, M.; Nagasawa, H.; Tsuru, T. Development of an Acetylacetonate-Modified Silica-Zirconia Composite Membrane Applicable to Gas Separation. *J. Membr. Sci.* **2020**, *599*, 117844.
29. Puthai, W.; Kanezashi, M.; Nagasawa, H.; Wakamura, K.; Ohnishi, H.; Tsuru, T. Effect of Firing Temperature on Water Permeability of SiO₂-ZrO₂ Membranes for Nanofiltration. *J. Membr. Sci.* **2016**, *497*, 348–356.
30. Puthai, W.; Kanezashi, M.; Nagasawa, H.; Tsuru, T. SiO₂-ZrO₂ Nanofiltration Membranes of Different Si/Zr Molar Ratios: Stability in Hot Water and Acid/Alkaline Solutions. *J. Membr. Sci.* **2017**, *524*, 700–711.
31. Lawal, S. O.; Takahashi, Y.; Nagasawa, H.; Tsuru, T.; Kanezashi, M. Microporous Structure Control of SiO₂-ZrO₂ Composite Membranes via Yttrium Doping and an Evaluation of Thermal Stability, *J. Sol-Gel Sci. Technol.* **2022**, *104*, 566–579.
32. Brett, R. B.; Wilsey, S.; Houk, K. N. The C₇H₁₀ Potential Energy Landscape: Concerted Transition States and Diradical Intermediates for the Retro-Diels–Alder Reaction and [1,3] Sigmatropic Shifts of Norbornene. *J. Am. Chem. Soc.* **1999**, *121*, 4816–4826.

- 625 33. Janiak, C.; Lassahn, P. G. The Vinyl Homopolymerization of Norbornene. *Macromol. Rapid*
626 *Commun.* **2001**, *22*, 479–492.
- 627 34. Sutthasupa, S.; Shiotsuki, M.; Sanda, F. Recent Advances in Ring-Opening Metathesis
628 Polymerization, and Application to Synthesis of Functional Materials. *Polym. J.* **2010**, *42*,
629 905–915.
- 630 35. Ogawa, K. A.; Goetz, A. E.; Boydston, A. J. Metal-Free Ring-Opening Metathesis
631 Polymerization. *J. Am. Chem. Soc.* **2015**, *137*, 1400–1403.
- 632 36. Lu, P.; Kensy, V. K.; Tritt, R. L.; Seidenkranz, D. T.; Boydston, A. J. Metal-Free Ring-
633 Opening Metathesis Polymerization: From Concept to Creation. *Acc. Chem. Res.* **2020**, *53*,
634 2325–2335.
- 635 37. Singleton, D. A; Schulmeier, B. E.; Hang, C.; Thomas, A. A.; Leung, S.-W.; Merrigan, S. R.
636 Isotope Effects and the Distinction Between Synchronous, Asynchronous, and Stepwise Diels–
637 Alder Reactions. *Tetrahedron* **2001**, *57*, 5149–5160.
- 638 38. Dong, X.; Duan, R.-T.; Ni, Y.-P.; Cao, Z.-J.; Chen, L.; Wang, Y.-Z. Fire Behavior of Novel
639 Imidized Norbornene-Containing Poly(ethylene terephthalate) Copolymers: Influence of
640 Retro-Diels-Alder Reaction at High Temperature. *Polym. Degrad. Stab.* **2017**, *146*, 105–112.
- 641 39. Ayiania, M.; Smith, M.; Hensley, A. J. R.; Scudiero, L.; McEwen, J.-S.; Garcia-Perez, M.
642 Deconvoluting the XPS Spectra for Nitrogen-Doped Chars: An Analysis from First Principles.
643 *Carbon* **2020**, *162*, 528–544.
- 644 40. Meng, D.; Yue, C.; Wang, T.; Chen, X. Evolution of Carbon Structure and Functional Group
645 During Shenmu Lump Coal Pyrolysis. *Fuel* **2021**, *287*, 119538.

41. Masse, S.; Laurent, G.; Babonneau, F. High Temperature Behavior of Periodic Mesoporous Ethanesilica Glasses Prepared from a Bridged Silsesquioxane and a Non-Ionic Triblock Copolymer. *J. Non-Cryst. Solids* **2007**, *353*, 1109–1119.
42. Tchoua Ngamou, P. H.; Ivanova, M. E.; Meulenberg, W. A. High-Performance Carbon Molecular Sieve Membranes for Hydrogen Purification and Pervaporation Dehydration of Organic Solvents. *J. Mater. Chem. A* **2019**, *7*, 7082–7091.
43. Lee, H. R.; Kanezashi, M.; Shimomura, Y.; Yoshioka, T.; Tsuru, T. Evaluation and Fabrication of Pore-Size-Tuned Silica Membranes with Tetraethoxydimethyl Disiloxane for Gas Separation. *AIChE J.* **2011**, *57*, 2755–2765.
44. Nagasawa, H.; Niimi, T.; Kanezashi, M.; Yoshioka, T.; Tsuru, T. Modified Gas Translation Model for Prediction of Gas Permeation through Microporous Organosilica Membranes. *AIChE J.* **2014**, *60*, 4199–4210.
45. Yoshioka, T.; Nakanishi, E.; Tsuru, T.; Asaeda, M. Experimental Studies of Gas Permeation through Microporous Silica Membranes. *AIChE J.* **2001**, *47*, 2052–2063.
46. Iyer, G. M.; Zhang, C. Precise Hydrogen Sieving by Carbon Molecular Sieve Membranes Derived from Solution-Processable Aromatic Polyamides. *ACS Mater. Lett.* **2023**, *5*, 243–248.
47. Araújo, T.; Parnell, A. J.; Bernardo, G.; Mendes, A. Cellulose-Based Carbon Membranes for Gas Separations – Unraveling Structural Parameters and Surface Chemistry for Superior Separation Performance. *Carbon* **2023**, *204*, 398–410.
48. Weng, Y.; Li, N.; Xu, Z.; Huang, J.; Huang, L.; Wang, H.; Li, J.; Wang, Y.; Ma, X. Super High Gas Separation Performance Membranes Derived from a Brominated Alternative PIM by Thermal Induced Crosslinking and Carbonization at Low Temperature. *Sep. Purif. Technol.* **2023**, *314*, 123548.

49. Hou, M.; Li, L.; He, Z.; Xu, R.; Lu, Y.; Wang, T. High Hydrogen Permselective Carbon Molecular Sieve Membrane and Its Structural Formation Mechanism. *Carbon* **2023**, *205*, 194–206.
50. Li, L.; Wang, C.; Wang, N.; Cao, Y.; Wang, T. The Preparation and Gas Separation Properties of Zeolite/Carbon Hybrid Membranes. *J. Mater. Sci.* **2015**, *50*, 2561–2570.
51. Xu, R.; He, L.; Li, L.; Hou, M.; Wang, Y.; Zhang, B.; Liang, C.; Wang, T. Ultraselective Carbon Molecular Sieve Membrane for Hydrogen Purification. *J. Energy Chem.* **2020**, *50*, 16–24.
52. He, W.; Du, J.; Liu, L.; Sun, Q.; Song, Z.; Ma, J.; Cao, D.; Lim, W.; Hassan, S. U.; Liu, J. Nanoarchitectonics of Carbon Molecular Sieve Membranes with Graphene Oxide and Polyimide for Hydrogen Purification. *RSC Adv.* **2023**, *13*, 10168–10181.
53. Kim, Y. K.; Park, H. B.; Lee, Y. M. Gas Separation Properties of Carbon Molecular Sieve Membranes Derived from Polyimide/Polyvinyl Pyrrolidone Blends: Effect of the Molecular Weight of Polyvinylpyrrolidone. *J. Membr. Sci.* **2005**, *251*, 159–167.
54. Kanezashi, M.; Matsutani, T.; Wakihara, T.; Hiromasa, T.; Hiroki, N.; Tomohisa, Y.; Tsuru, T. Tailoring the Subnano Silica Structure via Fluorine Doping for Development of Highly Permeable CO₂ Separation Membranes. *ChemNanoMat* **2016**, *2*, 264–267.
55. Kanezashi, M.; Yoneda, Y.; Nagasawa, H.; Tsuru, T. Gas Permeation Properties for Organosilica Membranes with Different Si/C Ratios and Evaluation of Microporous Structures. *AIChE J.* **2017**, *63*, 4491–4498.
56. Anggarini, U.; Yu, L.; Nagasawa, H.; Kanezashi, M.; Tsuru, T. Metal-Induced Microporous Aminosilica Creates a Highly Permeable Gas-Separation Membrane. *Mater. Chem. Front.* **2021**, *5*, 3029–3042.

57. Kusakabe, K.; Murata, A.; Kuroda, T.; Morooka, S. Preparation of MFI-Type Zeolite Membranes and Their Use in Separating n-Butane and i-Butane. *J. Chem. Eng. Jpn.* **1997**, *30*, 72–78.
58. Coronas, J.; Falconer, J. L.; Noble, R. D. Characterization and Permeation Properties of ZSM-5 Tubular Membranes. *AIChE J.* **1997**, *43*, 1797–1812.
59. Matsufuji, T.; Nishiyama, N.; Matsukata, M.; Ueyama, K. Separation of Butane and Xylene Isomers with MFI-Type Zeolitic Membrane Synthesized by a Vapor-Phase Transport Method. *J. Membr. Sci.* **2000**, *178*, 25–34.
60. Nouri, A.; Jafari, M.; Kazemimoghadam, M.; Mohammadi, T. Potential Separation of SF₆ from Air Using Chabazite Zeolite Membranes. *Chem. Eng. Technol.* **2014**, *37*, 317–324.
61. Sugiyama, Y.; Ikarugi, S.; Oura, K.; Ikeda, A.; Matsuyama, E.; Ono, R.; Nomura, M.; Tawarayama, H.; Saito, T.; Kuwahara, K. MFI Zeolite Membranes Prepared on Novel Silica Substrates. *J. Chem. Eng. Jpn.* **2015**, *48*, 891–896.
62. Tanizume, S.; Yoshimura, T.; Ishii, K.; Nomura, M. Control of Sequential MTO Reactions through an MFI-Type Zeolite Membrane Contactor. *Membranes* **2020**, *10*, 26–36.
63. Lan, L.; Wu, H.; Saulat, H.; Li, L.; Yang, J.; Lu, J. Synthesis of Ethanol Perm-Selective MFI Zeolite Membranes by Binary Structure Directing Agents. *J. Membr. Sci.* **2020**, *598*, 117647.
64. Kim, D. H.; Ko, Y. H.; Kim, T. H.; Park, J. S.; Lee, H. K. Separation of N₂/SF₆ Binary Mixtures Using Polyethersulfone (PESf) Hollow Fiber Membrane. *Korean J. Chem. Eng.* **2012**, *29*, 1081–1085.
65. Lee, S.; Suk, J.; Lee, M.; Choi, J.; Kim, S.; Lee, S. Separation of Sulfur Hexa Fluoride (SF₆) from Ternary Gas Mixtures Using Commercial Polysulfone (PSf) Hollow Fiber Membranes. *J. Membr. Sci.* **2014**, *452*, 311–318.

66. Dai, Y.; Li, Q.; Ruan, X.; Hou, Y.; Jiang, X.; Yan, X.; He, G.; Meng, F.; Wang, Z. Fabrication of Defect-Free Matrimid® Asymmetric Membranes and the Elevated Temperature Application for N₂/SF₆ Separation. *J. Membr. Sci.* **2019**, *577*, 258–265.

